



# Tectonic Context and Possible Triggering of the 2019–2020 Puerto Rico Earthquake Sequence

Marjolein Blasweiler<sup>1</sup>, Matthew W. Herman<sup>1,2</sup> , Fenna Houtsma<sup>1</sup>, and Rob Govers<sup>\*1</sup> 

## Abstract

An historically unprecedented seismic moment was released by crustal events of the 2019–2020 earthquake sequence near southwest Puerto Rico. The sequence involved at least two, and perhaps three interacting fault systems. The largest  $M_w$  6.4 event was likely triggered by left lateral strike-slip events along the eastern extension of the North Boquerón Bay-Punta Montalva fault zone. The mainshock occurred in a normal fault zone that extends into a region where previous studies documented extensional deformation, beyond the Ponce fault and the Bajo Tasmanian fault. Coulomb stress changes by the mainshock may have triggered further normal-faulting aftershocks, left lateral strike-slip events in the region where these two fault zones interacted, and possibly right lateral strike-slip aftershocks along a third structure extending southward, the Guayanilla fault zone. Extension directions of the seismic sequence are consistently north-northwest–south-southeast-oriented, in agreement with the Global Navigation Satellite Systems-inferred motion direction of eastern Hispaniola relative to western Puerto Rico, and with crustal stress estimates for the overriding plate boundary zone.

**Cite this article as** Blasweiler, M., M. W. Herman, F. Houtsma, and R. Govers (2022). Tectonic Context and Possible Triggering of the 2019–2020 Puerto Rico Earthquake Sequence, *Seismol. Res. Lett.* **93**, 584–593, doi: [10.1785/0220210224](https://doi.org/10.1785/0220210224).



[Supplemental Material](#)

## Introduction

The Caribbean–North American plate boundary zone between the island of Hispaniola (Haiti and Dominican Republic) and the U.S. Virgin Islands accommodates highly oblique left-lateral relative motion at 18–20 mm/yr (DeMets *et al.*, 2007, 2010; Calais *et al.*, 2016; Fig. 1). Near Puerto Rico, the plate boundary zone has a north–south extent of ~100–200 km and is bounded in the north by the Puerto Rico trench and by the Muertos trough and Anageda fault in the south (Mann *et al.*, 1995, 2002; Calais *et al.*, 2002, 2010; Jansma and Mattioli, 2005). Relative motions and crustal deformation of the overriding Caribbean plate vary across the plate boundary zone (Jansma *et al.*, 2000; Manaker *et al.*, 2008; Benford *et al.*, 2012; Symithe *et al.*, 2015). Shear coupling of the subducting North American plate and the overriding plate boundary zone is variable (Symithe *et al.*, 2015); it is significant near Hispaniola where oblique convergence is accompanied by strain partitioning, and coupling is weak further to the east without strain partitioning (Calais *et al.*, 2016). The east–west extension occurs in the Mona Passage (Chaytor and ten Brink, 2010; Mondziel *et al.*, 2010), where the coupling between the slab and overriding plate changes.

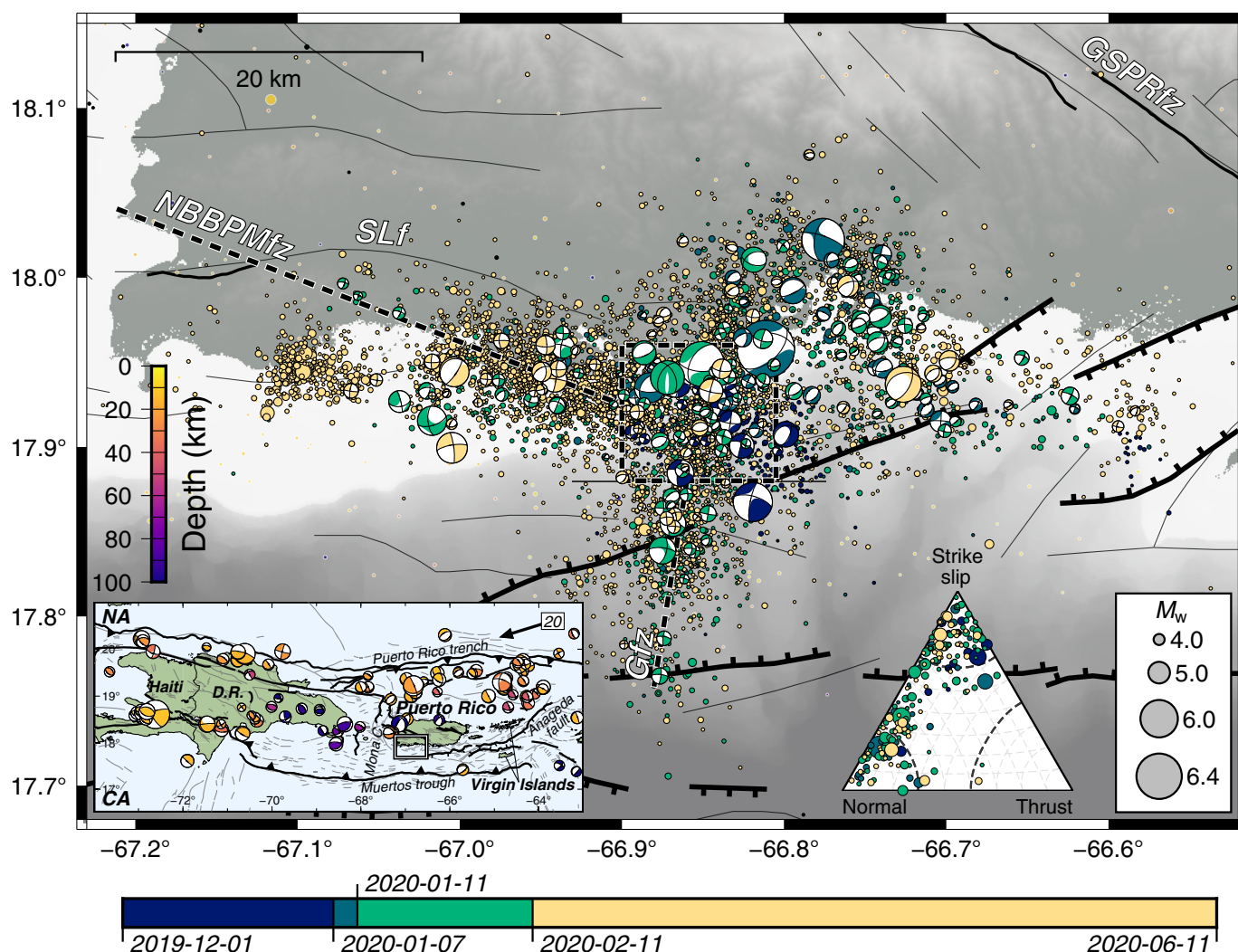
The 2019–2020 earthquake sequence occurred ~60 km east of Mona Passage along the western side of the south coast of Puerto Rico. According to the U.S. Geological Survey (USGS)

Comprehensive Catalog (ComCat, 2021), which reports the earthquake locations determined by the Puerto Rico Seismic Network (PRSN; see [Data and Resources](#)), the earthquake depths dominantly ranged from 5 to 20 km. The sequence involved 13  $M_w > 4.9$  earthquakes from 28 December 2019 to 7 July 2020. The largest event ( $M_w$  6.4) occurred on 7 January 2020, following an  $M_w$  5.0 on 28 December 2019 and an  $M_w$  5.8 on 6 January 2020 (López *et al.*, 2020). The earthquakes were located within a diffuse zone of smaller magnitude seismicity to the south-southwest of the Great Southern Puerto Rico fault zone (Huérffano *et al.*, 2005). Since 1974, 27  $M_w \geq 4$  earthquakes have been recorded south and southeast of Mona Canyon, and the largest recorded crustal event before 2019 was the  $M_w$  5.2 earthquake of 2011 in the south Mayagüez basin. The last significant earthquake in the region occurred on 13 November 1999, had a hypocenter at 17 km depth directly south-southwest of Guánica, and had a magnitude of 4.1. Prior to this, the 30 May 1987  $M_w$  4.6 Cabo Rojo event had a hypocentral depth of 5 km. It is particularly the

1. Tectonophysics Group, Faculty of Geosciences, Utrecht University, Netherlands,  <https://orcid.org/0000-0003-4684-9459> (MWH);  <https://orcid.org/0000-0001-7148-8857> (RG); 2. Department of Geological Sciences, California State University, Bakersfield, Bakersfield, California, U.S.A.

\*Corresponding author: [rgovers@uu.nl](mailto:rgovers@uu.nl)

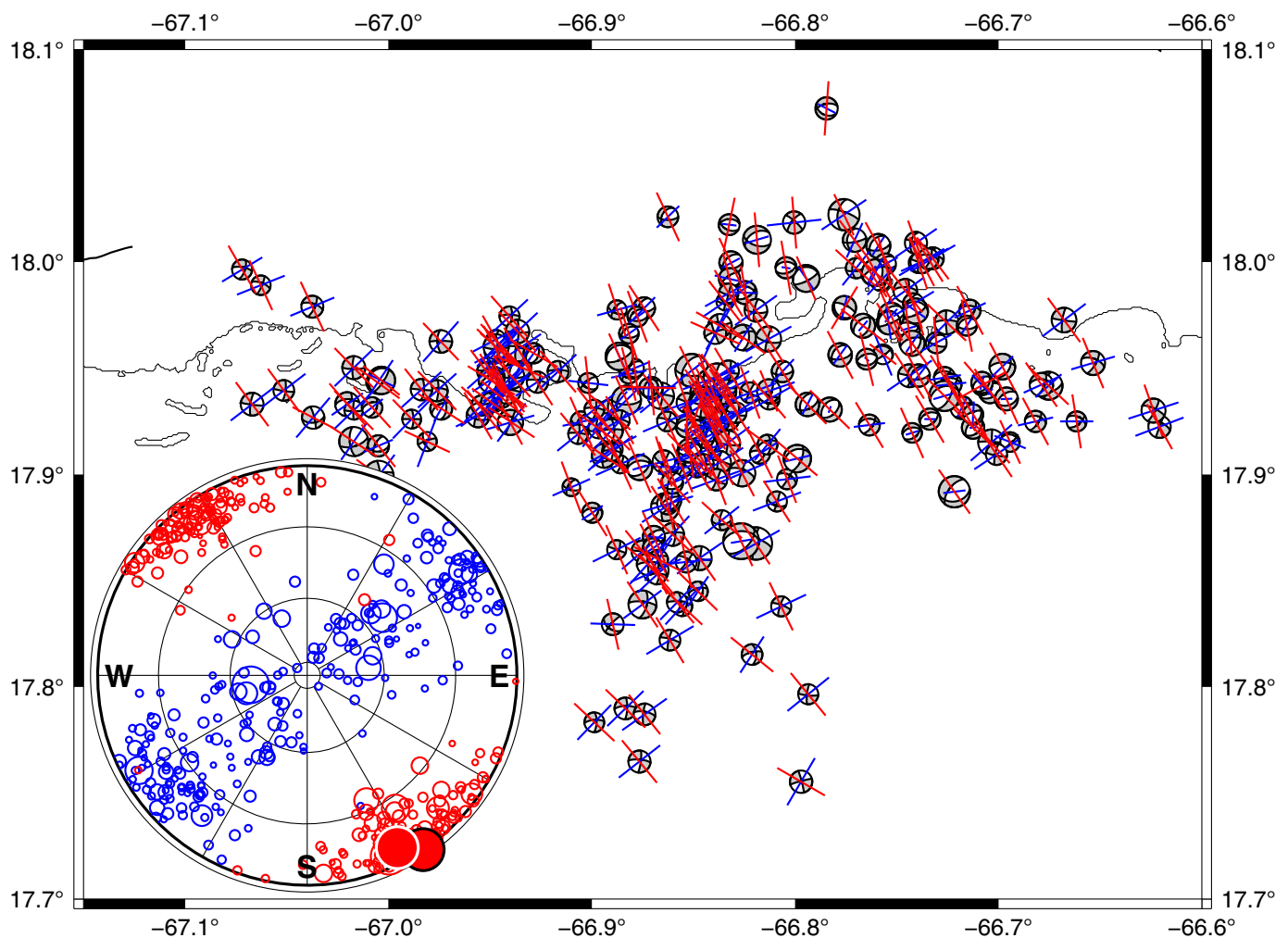
© Seismological Society of America



high magnitudes of the shallow crustal events in the 2019–2020 sequence that had not previously been observed.

Various studies have addressed the question of which active faults accommodate the relative motion between the western (Hispaniola) and eastern (Puerto Rico–Virgin Islands) parts of the plate boundary zone. Trenching along the western South Lajas fault (SLf) showed recent normal faulting and transform faulting (Prentice *et al.*, 2000; Prentice and Mann, 2005), but activity on its eastern extent is poorly constrained. Roig-Silva *et al.* (2013) interpreted a variety of surface observations in favor of dominant activity on the North Boquerón Bay–Punta Montalva fault zone (NBBPMfz). Overall, the NBBPMfz accommodates left-lateral relative motions but has small northeast-striking normal fault segments. Offshore seismic profiling in Boquerón Bay indicates that the NBBPMfz is no longer active off the western coast of Puerto Rico (Grindlay *et al.*, 2005). Surface fault offsets in the east-southeast near the 2019–2020 seismogenic region appear to be young and significant (Granja Bruña *et al.*, 2015) and marine geophysical studies along the Puerto Rico south coast show normal faults (Beach and Trumbull, 1981; van Gestel *et al.*, 1998).

**Figure 1.** (Inset) The Caribbean–North American plate boundary zone between the Dominican Republic and the U.S. Virgin Islands. The region of the 2019–2020 earthquake sequence is indicated by the box. Historical moment tensors from the Global Centroid Moment Tensor catalog are shown scaled by magnitude and colored by depth. Faults from Styron and Pagani (2020) are plotted with bold lines, and faults from French and Schenk (2004) are shown as lighter gray lines. The relative Caribbean–North American plate motion is 18–20 mm/yr (DeMets *et al.*, 2007), with the direction indicated by an arrow. Seismotectonics of the 2019–2020 earthquake sequence region. Historical seismicity (1990–2018) from ComCat is shown as white-outlined circles, scaled by magnitude, and colored by depth. Seismicity from 2019 to 2020 and moment tensors from ComCat have black outlines and are colored by date of occurrence. Offshore normal faults are from Granja Bruña *et al.* (2015), and the North Boquerón Bay–Punta Montalva fault zone (NBBPMfz) is from Roig-Silva *et al.* (2013). The complex fault intersection region is highlighted by a dashed box, and the Guayanilla fault zone (Gfz; this study) extends from this intersection zone to the south. Other potentially relevant or significant faults include the South Lajas fault (SLf) and Greater Southern Puerto Rico fault zone (GSPRFz). The color version of this figure is available only in the electronic edition.



The most recently published block model of interseismic Global Navigation Satellite Systems (GNSS) velocities (Symithe *et al.*, 2015) supports the conclusion of earlier studies that the Puerto Rico-Virgin Islands microplate moves slowly relative to the Caribbean plate. According to this model, the Hispaniola microplate moves away from Puerto Rico toward the west-northwest (azimuth:  $\sim 300^\circ$ ) at a rate of  $\sim 3$  mm/yr. The maximum fault slip during the 7 January 2020  $M_w$  6.4 event was  $\sim 1.6$  m (Liu *et al.*, 2020). Assuming that this fault is the only active structure, it would require  $>500$  yr to accumulate such slip deficit. However, given the distributed nature of the fault zone and numerous, different styles of active faults in the region, it likely took substantially longer to accumulate the deformation responsible for driving the earthquake sequence. It is thus unsurprising that similar or higher magnitude events were not documented previously.

ComCat also includes teleseismic W-phase moment tensor solutions for the  $M_w > \approx 4.6$  earthquakes, and regional double-couple solutions for  $M_w > \approx 3.1$  earthquakes that occurred during the seismic sequence. The T axes of the 2019–2020 seismic sequence are almost uniformly oriented north-northwest–south-southeast (Fig. 2), roughly in agreement with the GNSS-

**Figure 2.** Earthquake P and T axes for 239 events in the 2019–2020 sequence with focal mechanisms from ComCat. The map shows the earthquake focal mechanisms in gray, with the horizontal projections of unit P axes (blue) and unit T axes (red). The inset plot is a stereographic plot showing the earthquake P axes (blue) and T axes (red) with symbol size scaled by earthquake magnitude. The large black-outlined dot shows the location of the mean T axis and the white-outlined dot shows the moment-weighted mean T axis, which show the dominance of south-southeast extension in the sequence. The color version of this figure is available only in the electronic edition.

inferred relative motion direction of east Hispaniola relative to Puerto Rico and with the direction of maximum extensional crustal strain and tensional deviatoric stress estimates (van Benthem and Govers, 2010). The tectonic context and the earthquake-faulting mechanisms suggest that at least two main faults were active in the sequence, and likely more. Left-lateral strike-slip events occurred on west-northwest-striking faults parallel to (but offset south of) the NBBPMfz. A series of normal-faulting events including the  $M_w$  6.4 earthquake occurred to the east, south of the coast in the extensional region where

TABLE 1

**Fault Planes of the 11  $M_w$  5+ Earthquakes in the Sequence from December 2019 to July 2020**

Origin Time (yyyy/mm/dd)	Magnitude	Nodal Plane 1	Nodal Plane 2	Interpretation
2019/12/29	5.0	290/80/–10	22/80/–170	NBBPMfz
2020/01/06	5.8	290/80/–10	22/80/–170	NBBPMfz
2020/01/07	6.4	47/54/–116	268/43/–58	Normal
2020/01/07	5.6	80/37/–55	218/60/–114	Normal
2020/01/07	5.0	190/60/–136	77/53/39	Normal
2020/01/07	5.6	300/80/5	209/85/170	?
2020/01/10	5.2	221/45/–135	95/60/–55	Oblique normal fault in intersection zone
2020/01/11	5.9	233/56/–113	90/40/–60	Oblique normal fault in intersection zone
2020/01/15	5.2	75/85/–20	167/70/–175	NBBPMfz
2020/01/25	5.0	107/56/–58	239/45/–128	Normal
2020/02/04	5.0	276/72/–27	14/65/–161	Gfz
2020/05/02	5.4	28/60/–114	251/38/–54	Normal
2020/07/03	5.3	260/75/–10	353/80/–165	NBBPMfz

Gfz, Guayanilla fault zone; NBBPMfz, North Boquerón Bay-Punta Montalva fault zone.

Granja Bruña *et al.* (2015) identified fault traces. The subsequent aftershocks occurred on these main faults as well as several other nearby faults. The earthquake sequence can thus be seen as activity on multiple interacting fault zones in response to horizontal deviatoric tectonic stresses. We seek to further characterize these interactions and triggering using coulomb stress change analysis.

## Seismicity and Active Faulting

Uncertainties in the hypocenters and in the location and dip of regional faults preclude a definitive identification of the faults that were active during the 2019–2020 sequence. However, by combining the earthquake locations and faulting mechanisms with the temporal distribution of seismicity (Fig. 1; see also the Animation file, available in the supplemental material to this article; Table 1), some patterns start to emerge. The sequence began with a series of strike-slip events up to  $M_w$  5.8 along the eastern extension of the NBBPMfz, ~5 km south of the SLf (Fig. 1). Based on their locations and south-southeast-oriented distribution we would interpret these events as dominantly left-lateral strike-slip earthquakes, but later seismicity throws this simple interpretation into question. The 7 January 2020  $M_w$  6.4 mainshock epicenter was located ~3 km south of the eastern end of this precursory sequence. We are not able to confidently identify which nodal plane of the mainshock is the fault plane from the aftershocks alone; however, Liu *et al.* (2020) and Nobile *et al.* (2021) found that they could better fit seismic and geodetic observations with a north-dipping plane. When we model the horizontal coseismic surface offsets

(using the equations of Okada, 1992 and the empirical relations of Wells and Coppersmith, 1994, and Allen and Hayes, 2017), the fit is not greatly improved by the choice of fault plane and is instead more sensitive to the earthquake location and fault dimensions (Fig. S1). Based on the previously published work, we use the north-dipping plane as the fault plane for our main analysis, but we also show results for the other nodal plane.

This mainshock was followed shortly after by vigorous normal-faulting aftershock activity to the east-northeast, several strike-slip earthquakes up to  $M_w$  4.4 on the NBBPMfz west of the initial sequence, and an  $M_w$  5.6 strike-slip event onshore southern Puerto Rico. On 10 January 2020, an  $M_w$  5.2 oblique normal-faulting earthquake occurred at the western end of the initial sequence, and 12 hr later an  $M_w$  5.9 earthquake with a similar focal mechanism occurred. These oblique events were quickly followed by a series of dominantly strike-slip events along what appears to be a previously unmapped north-north-east-striking fault zone south of the NBBPMfz. We refer to this tentatively interpreted fault zone as the Guayanilla fault zone (Gfz), and it would be a right-lateral system conjugate to the NBBPMfz. Finally, several smaller strike-slip events occurred west of the entire sequence. As the aftershock activity decayed over the next few months, this distribution of aftershock activity remained nearly stationary (see the Animation file in supplemental material). The majority of earthquakes, the greatest moment release, and the widest variety of focal mechanisms in the 2019–2020 sequence occurred in the intersection zone between the NBBPMfz and Gfz (indicated by the dashed box in Fig. 1).



To determine which faults were the major contributors to the deformation in the sequence, we calculate the seismic moment released by fault. The initial events prior to the  $M_w$  6.4 mainshock were dominated by strike-slip ( $5.0 \times 10^{17}$  N·m) faulting, with secondary normal faulting ( $2.0 \times 10^{16}$  N·m) and minor oblique normal faulting ( $1.6 \times 10^{15}$  N·m). The normal-faulting mainshock was  $M_w$  6.4, or  $5.0 \times 10^{18}$  N·m, and subsequent normal-faulting aftershocks accounted for  $6.4 \times 10^{17}$  N·m. Although we cannot identify the causative faults for events in the intersection zone between the NBBPMfz and Gfz (Fig. 1), this region was highly active, releasing  $9.3 \times 10^{17}$  N·m of strike-slip and oblique seismic moment. Outside of the fault intersection region, the greatest strike-slip moment release was associated with the  $M_w$  5.6 event that occurred onshore at the northern end of the sequence ( $7.4 \times 10^{17}$  N·m). The western side of the sequence on the NBBPMfz also had robust aftershock moment release ( $2.9 \times 10^{17}$  N·m). In contrast, although there were numerous aftershocks on the southern extension of the Gfz, only  $8.0 \times 10^{16}$  N·m of seismic moment were released there. These results suggest that most of the moment release resulted from distributed normal faulting on structures similar to those previously mapped offshore, as well as strike-slip faulting along the NBBPMfz and particularly where it intersects with the Gfz. Secondary moment release occurred on the Gfz and on faults west of Punta Montalva and south of the NBBPMfz.

## Coulomb Stress Change Modeling

To assess the role of the largest earthquakes in the sequence triggering subsequent events, we compute coulomb stress changes ( $\Delta CS = \tau - \mu \sigma_n$ , in which  $\tau$  is the shear stress change and  $\sigma_n$  is the normal stress change resolved on a target fault, and  $\mu$  is the static coefficient of friction; Reasenber and Simpson, 1992; Stein *et al.*, 1992). The modeling is based on the approach of Herman *et al.* (2016). The stress changes caused by each earthquake source are calculated using the analytical solutions for uniform slip on a rectangular fault in a uniform isotropic elastic half space (Okada, 1992). The half-space has a shear modulus of 40 GPa and a Poisson's ratio of 0.25 (reasonable values for crustal rocks that scale the stress magnitudes; e.g., Herman and Furlong, 2016; Herman *et al.*, 2016). We resolve  $\Delta CS$  on relevant target fault planes, using a static friction coefficient of 0.5. We calculate  $\Delta CS$  at the locations of each event of interest (using both the PRSN locations and the locations determined by Cromwell *et al.*, 2021), and for plotting we show the  $\Delta CS$  along a horizontal plane at the average depth of the earthquakes in the sequence from the corresponding catalog. Our interpretation is that faults with a positive  $\Delta CS$  are brought closer to brittle shear failure, whereas a negative  $\Delta CS$  implies that a fault is inhibited from slipping. If we find that events in the sequence preferentially occur in regions of positive  $\Delta CS$  produced by prior earthquakes, we can infer from this that the previous seismicity triggered the subsequent

events. If instead earthquakes do not systematically occur in areas of positive  $\Delta CS$ , some other process is likely to be driving their occurrence.

The source fault orientations, dimensions, and slip are determined from the USGS moment tensors. We select the fault kinematics from the best-fitting double couple, use an empirical relation (Allen and Hayes, 2017) to determine the fault dimensions, and calculate the fault slip from the seismic moment equation (Kanamori, 1977). The rectangular fault-slip patch is centered on the hypocenter from the earthquake catalog. To evaluate triggering of aftershocks by the mainshock source, we also test the sensitivity to using the Liu *et al.* (2020) slip model, which is based on a combination of local strong motion, teleseismic broadband, and static GNSS displacement observations.

We assume that events prior to the  $M_w$  6.4 mainshock are left-lateral strike-slip and calculate the  $\Delta CS$  on normal faults like the mainshock (the results for our preferred north-dipping mainshock are shown in Fig. 3, and those for a southeast-dipping mainshock in Fig. S2). The assumption that these events are left lateral does not change the  $\Delta CS$  results significantly because the earthquakes are sufficiently small magnitude ( $M_w \leq 5.8$ ) that their fault area is small. We find that the hypocenter of the 7 January mainshock is likely positively loaded by these events, occurring in a region where  $\Delta CS$  is +0.02 MPa (using PRSN locations; Fig. 3a) to +0.43 MPa (using the locations of Cromwell *et al.*, 2021; Fig. 3b). The mainshock location consequently differs in Figure 3a,b. Based on these highest-quality locations available, we conclude that the  $M_w$  6.4 mainshock was positively loaded by the preceding events. From tests of the  $\Delta CS$  sensitivity to the mainshock location, we find that (1) the  $M_w$  6.4 can be moved into a region of negative  $\Delta CS$  within location uncertainties, but (2) if the  $M_w$  6.4 hypocenter is deeper than the initial strike-slip events—as the high-quality locations suggest—then it is robustly in a region of positive  $\Delta CS$ . We also find that the results are more sensitive to earthquake location than to the choice of empirical relation used for determining the fault areas of the initial seismicity.

The  $\Delta CS$  generated by the mainshock is first calculated assuming a uniform slip rectangular fault centered on the PRSN hypocenter, using the empirical relations of Allen and Hayes (2017) (Fig. 4). There are small variations in the  $\Delta CS$  distribution for normal and strike-slip target planes, shifting positive and negative regions by up to 3 km near the fault edges. However, the regional pattern of  $\Delta CS$  at shallow seismogenic depths (8 km) is similar for both strike-slip and normal target faults: positive  $\Delta CS$  loading off the east and west sides of the fault, and negative  $\Delta CS$  loading north, south, and on top of the fault. The consequence of this  $\Delta CS$  distribution is that the normal-faulting and strike-slip aftershocks to the northeast of the mainshock are located in an area of  $\Delta CS$  magnitudes >0.10 MPa, but with high uncertainty in the sign of

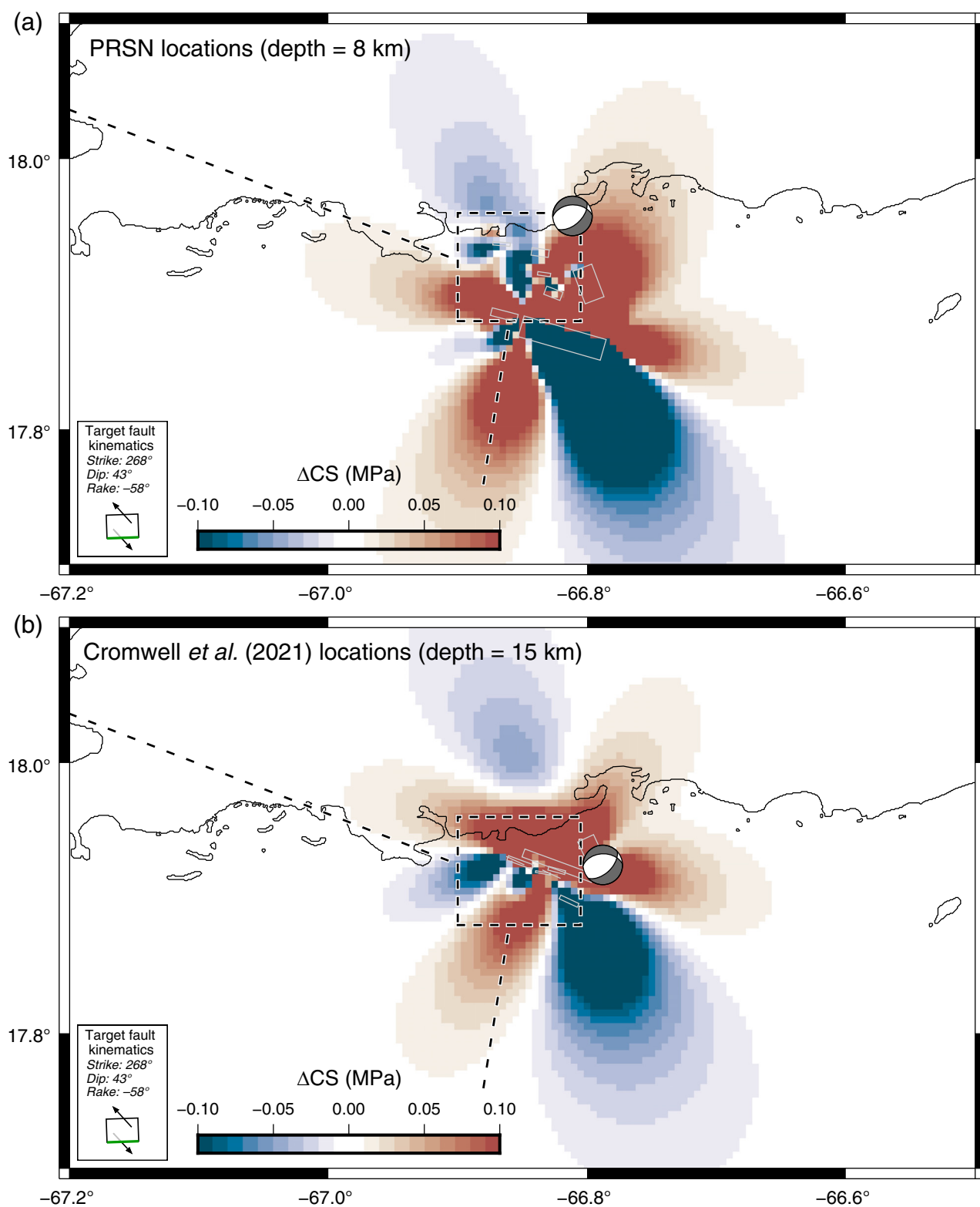


**Figure 3.** Coulomb stress changes generated by the seven  $M_w$  4.5 + events prior to the 7 January 2020  $M_w$  6.4 mainshock using (a) the Puerto Rico Seismic Network (PRSN) hypocenter locations, and (b) the locations of [Cromwell et al. \(2021\)](#). The horizontal projections of source faults are indicated by light gray rectangles.  $\Delta CS$  are calculated on target faults with the same orientation as the north-dipping fault plane of the  $M_w$  6.4 mainshock. The vertical locations of these target faults are taken to coincide with

the hypocentral depth of the mainshock (8 km for the PRSN solution or 15 km for the [Cromwell et al., 2021](#), solution), and we compute the  $\Delta CS$  on a uniform horizontal grid at this depth. The  $M_w$  6.4 epicenter is shown by the focal mechanism. The locations of the NBBPMfz, the Gfz, and the fault intersection zone (from Fig. 1) are shown as dashed lines. The color version of this figure is available only in the electronic edition.

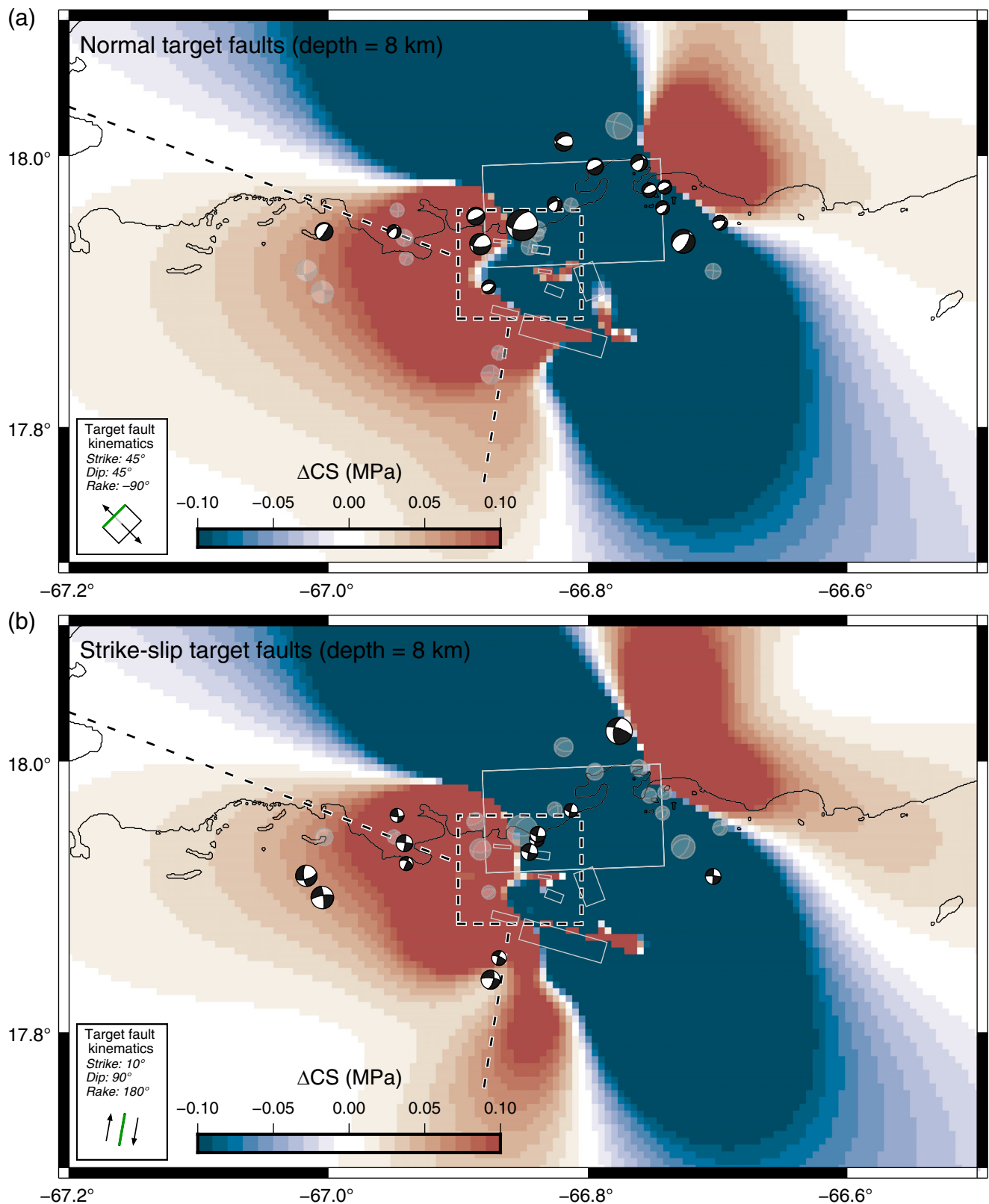


**Figure 4.** Coulomb stress changes on a horizontal plane at 8 km depth generated by the initial events and the mainshock assuming uniform slip on a north-dipping rectangular fault at the PRSN hypocenter. The horizontal projections of source faults are indicated by light gray rectangles. The locations of the NBBPMfz, the Gfz, and the fault intersection zone (from Fig. 1) are shown as

dashed lines. (a)  $\Delta CS$  resolved onto normal-faulting target faults shown by focal mechanisms (strike-slip events are transparent). (b)  $\Delta CS$  resolved onto strike-slip target faults (focal mechanism plots), with normal events shown as transparent focal mechanisms. The color version of this figure is available only in the electronic edition.

the  $\Delta CS$  due to the proximity to the fault edge. Similarly, the aftershocks in the intersection zone have high- $\Delta CS$  magnitudes and uncertain  $\Delta CS$  signs because they are so close to the mainshock fault edge. The strike-slip events on the far western end of the sequence are robustly in a positive  $\Delta CS$  lobe. A similar result is produced using the locations of [Cromwell et al. \(2021\)](#) (Fig. S3), and is largely insensitive to the choice of the north- or south-dipping nodal plane for the  $M_w$  6.4 mainshock (Fig. S4).

If we use the finite-fault model of [Liu et al. \(2020\)](#)—also occurring on a north-dipping fault plane and located near the PRSN hypocenter—as the mainshock source, the pattern of  $\Delta CS$  changes mostly near the fault (Fig. S5). The primary difference is that a local low-slip zone in the center of the rupture zone results in a region of positive  $\Delta CS$  in the middle of the fault footprint. This puts some of the aftershocks in the intersection zone that were previously negatively loaded into zones of positive  $\Delta CS$ . From these analyses of the mainshock stress changes, we can conclude that the  $\Delta CS$  resolved onto the aftershocks in the center of the 2020 sequence is too sensitive to event locations and the mainshock slip distribution to robustly determine whether these events are positively or negatively loaded. Nevertheless, the systematic progression of the sequence with subsequent events generally occurring near the edges of preceding events (i.e., in areas of high- $\Delta CS$  magnitude) does strongly suggest a static stress change triggering mechanism. This interpretation is similar to aftershock sequences from other similar magnitude events occurring in intraplate settings ([Herman and Furlong, 2016](#); [Pananont et al., 2017](#)).

Finally, we consider the effects of subsequent large aftershocks on the pattern of  $\Delta CS$ . Although these events locally modify the stress field, their stress changes are too small compared to those of the  $M_w$  6.4 mainshock to have a significant impact on the regional stress change distribution. For example, if we add the aftershocks of the  $M_w$  6.4 through the 11 January 2021  $M_w$  5.9 earthquake to the  $\Delta CS$  calculation, the regional stress changes are largely unaltered (Fig. S6). Because the regional stress changes are so similar with or without the aftershocks through the 11 January event, our interpretations of whether later aftershocks are triggered or not remain the same. Even including all of the significant aftershocks (through the 3 July 2020  $M_w$  5.3 event) in the  $\Delta CS$  calculation, the total change to the regional stress field from this sequence is broadly similar to that of the  $\Delta CS$  through the mainshock only (Fig. S7). Therefore, in this case the  $M_w$  6.4 mainshock  $\Delta CS$  alone dominates the stress changes after its occurrence, although the aftershocks do modify the stress field locally, particularly near the fault edges where the stress changes are greatest.

## Discussion and Conclusions

From a historical perspective, the moment release of the crustal events of the 2019–2020 seismic sequence was exceptional for southwest Puerto Rico. Despite the faulting complexity of the

sequence, all of the events fit into the seismotectonic context of the region (e.g., [Grindlay et al., 2005](#); [Prentice and Mann, 2005](#); [van Benthem and Govers, 2010](#); [Roig-Silva et al., 2013](#); [Ganja Bruña et al., 2015](#)). Horizontal T axes of the events agree with regional stress directions and with the GNSS-inferred motion direction (and the corresponding maximum extensional strain direction) of eastern Hispaniola relative to Puerto Rico ([Jansma et al., 2000](#); [Jansma and Mattioli, 2005](#)). It is common for events near-fault edges to have highly negative  $\Delta CS$  values, that change  $\Delta CS$  sign with varying the event location within its uncertainty ([Herman and Furlong, 2016](#); [Herman et al., 2016](#); [Meade et al., 2017](#)). The limited resolution of the source fault-slip model, earthquake (i.e., target fault) locations, and earth structure preclude robust determination of regions with increased and decreased  $\Delta CS$ , and consequently of earthquake triggering relations. The largest  $M_w$  6.4 event was likely triggered by strike-slip events along the eastern extension of the NBBPMfz, particularly if it is located deeper than the initial strike-slip events. The mainshock occurred in a normal fault zone that extends beyond the Ponce fault and the Bajo Tasmanian fault.  $\Delta CS$  by the mainshock may have triggered further normal-faulting aftershocks, left-lateral strike-slip events, and right-lateral strike-slip events, particularly in the region where these fault zones interacted, and possibly along the southward-extending Gfz.

## Data and Resources

Seismic data come from ComCat (doi: [10.5066/F7MS3QZH](#)), which reports the Puerto Rico Seismic Network locations (PRSN, doi: [10.7914/SN/PR](#)). Figures S1–S7 and our animation of the 2019–2020 Puerto Rico earthquake sequence are available in the supplemental materials. The software for computing coseismic stress changes is available online (doi: [10.5281/zenodo.3894137](#)). Input and output files that were used for the models and figures of this article are digitally stored in the Yoda repository of Utrecht University (doi: [10.24416/UU01-15E13S](#)), in compliance with Findability, Accessibility, Interoperability, and Reuse of digital assets (FAIR) principles. Figures were made with GMT6 ([Wessel et al., 2019](#)).

## Declaration of Competing Interests

The authors acknowledge that there are no conflicts of interest recorded.

## Acknowledgments

The authors appreciate helpful reviews from two anonymous reviewers and the Guest Editor. The authors thank Thorne Lay and Chengli Liu for sharing their finite-slip solution of the  $M_w$  6.4 event. R. G. was partially supported by grant NWO-ALWGO.2017.007. Author contributions following the CRediT taxonomy: conceptualization: M. H. and R. G.; software: M. H.; investigation: F. H., M. B., and M. H.; resources: data curation: M. H.; writing-original draft: M. B., M. H., F. H., and R. G.; revised manuscript: M. H. and R. G.; visualization: M. B., F. H., and M. H.; supervision: R. G. and M. H.



## References

- Allen, T. I., and G. P. Hayes (2017). Alternative rupture-scaling relationships for subduction interface and other offshore environments, *Bull. Seismol. Soc. Am.* **107**, no. 3, 1240–1253, doi: [10.1785/0120160255](https://doi.org/10.1785/0120160255).
- Beach, D. K., and J. V. Trumbull (1981). Marine geologic map of the Puerto Rico insular shelf, Isla Caja de Muertos area, IMAP 1265, doi: [10.3133/i1265](https://doi.org/10.3133/i1265).
- Benford, B., C. DeMets, and E. Calais (2012). GPS estimates of microplate motions, northern Caribbean: Evidence for a Hispaniola microplate and implications for earthquake hazard, *Geophys. J. Int.* **191**, no. 2, 481–490, doi: [10.1111/j.1365-246x.2012.05662.x](https://doi.org/10.1111/j.1365-246x.2012.05662.x).
- Calais, E., A. Freed, G. Mattioli, F. Amelung, S. Jónsson, P. Jansma, S.-H. Hong, T. Dixon, C. Prepetit, and R. Momplaisir (2010). Transpressional rupture of an unmapped fault during the 2010 Haiti earthquake, *Nat. Geosci.* **3**, no. 11, 794–799, doi: [10.1038/ngeo992](https://doi.org/10.1038/ngeo992).
- Calais, E., Y. Mazabraud, B. M. de Lépinay, P. Mann, G. Mattioli, and P. Jansma (2002). Strain partitioning and fault slip rates in the northeastern Caribbean from GPS measurements, *Geophys. Res. Lett.* **29**, no. 18, 3–1–3–4, doi: [10.1029/2002gl015397](https://doi.org/10.1029/2002gl015397).
- Calais, E., S. Symithe, B. M. de Lépinay, and C. Prépetit (2016). Plate boundary segmentation in the northeastern Caribbean from geodetic measurements and Neogene geological observations. *C. R. Geosci.* **348**, no. 1, 42–51, doi: [10.1016/j.crte.2015.10.007](https://doi.org/10.1016/j.crte.2015.10.007).
- Chaytor, J. D., and U. S. ten Brink (2010). Extension in Mona passage, northeast Caribbean, *Tectonophysics*, **493**, nos. 1/2, 74–92, doi: [10.1016/j.tecto.2010.07.002](https://doi.org/10.1016/j.tecto.2010.07.002).
- ComCat (2021) Advanced National Seismic System (ANSS) comprehensive catalog of earthquake events and products, U.S. Geological Survey, Earthquake Hazards Program, doi: [10.5066/F7MS3QZH](https://doi.org/10.5066/F7MS3QZH).
- Cromwell, C. W., K. P. Furlong, E. A. Bergman, H. M. Benz, W. L. Yeck, and M. Herman (2021). Seismotectonic analysis of the 2019–2020 Puerto Rico sequence: The value of absolute earthquake relocations in improved interpretations of active tectonics, *Seismol. Res. Lett.* doi: [10.1785/0220210238](https://doi.org/10.1785/0220210238).
- DeMets, C., R. G. Gordon, and D. F. Argus (2010). Geologically current plate motions, *Geophys. J. Int.* **181**, no. 1, 1–80, doi: [10.1111/j.1365-246X.2009.04491.x](https://doi.org/10.1111/j.1365-246X.2009.04491.x).
- DeMets, C., G. S. Mattioli, P. Jansma, R. Rogers, C. Tenorios, and H. L. Turner (2007). Present motion and deformation of the Caribbean plate: Constraints from new GPS geodetic measurements from Honduras and Nicaragua, in *Geologic and Tectonic Development of the Caribbean Plate in Northern Central America*, P. Mann (Editor), Vol. 428, Geological Society of America, Boulder, Colorado, Special Paper, 21–36, doi: [10.1130/2007.2428\(02\)](https://doi.org/10.1130/2007.2428(02)).
- French, C. D., and C. J. Schenk (2004). Map showing geology, oil and gas fields, and geologic provinces of the Caribbean region, U.S. Geol. Surv. Open-File Rept. 97-470-K, doi: [10.3133/ofr97470K](https://doi.org/10.3133/ofr97470K).
- Granja Bruña, J. L. G., U. S. ten Brink, A. Muñoz-Martín, A. Carbó-Gorosabel, and P. L. Estrada (2015). Shallower structure and geomorphology of the southern Puerto Rico offshore margin, *Marine Pet. Geol.* **67**, 30–56, doi: [10.1016/j.marpetgeo.2015.04.014](https://doi.org/10.1016/j.marpetgeo.2015.04.014).
- Grindlay, N. R., L. J. Abrams, L. D. Greco, and P. Mann (2005). Toward an integrated understanding of Holocene fault activity in western Puerto Rico: Constraints from high-resolution seismic and sidescan sonar data, in *Active Tectonics and Seismic Hazards of Puerto Rico, the Virgin Islands, and Offshore Areas*, P. Mann (Editor), Geological Society of America, Boulder, Colorado, doi: [10.1130/0-8137-2385-x.139](https://doi.org/10.1130/0-8137-2385-x.139).
- Herman, M. W., and K. P. Furlong (2016). Revisiting the Canterbury earthquake sequence after the 14 February 2016 Mw 5.7 event, *Geophys. Res. Lett.* **43**, no. 14, 7503–7510, doi: [10.1002/2016gl069528](https://doi.org/10.1002/2016gl069528).
- Herman, M. W., K. P. Furlong, G. P. Hayes, and H. M. Benz (2016). Foreshock triggering of the 1 April 2014 Mw 8.2 Iquique, Chile, earthquake, *Earth Planet. Sci. Lett.* **447**, 119–129, doi: [10.1016/j.epsl.2016.04.020](https://doi.org/10.1016/j.epsl.2016.04.020).
- Huérffano, V., C. von Hillebrandt-Andrade, and G. Báez-Sánchez (2005). Microseismic activity reveals two stress regimes in southwestern Puerto Rico, in *Active Tectonics and Seismic Hazards of Puerto Rico, the Virgin Islands, and Offshore Areas*, P. Mann (Editor), Geological Society of America, Boulder, Colorado, doi: [10.1130/0-8137-2385-x.81](https://doi.org/10.1130/0-8137-2385-x.81).
- Jansma, P. E., and G. S. Mattioli (2005). GPS results from Puerto Rico and the Virgin Islands: Constraints on tectonic setting and rates of active faulting, in *Active Tectonics and Seismic Hazards of Puerto Rico, the Virgin Islands, and Offshore Areas*, P. Mann (Editor), Geological Society of America, Boulder, Colorado, doi: [10.1130/0-8137-2385-x.13](https://doi.org/10.1130/0-8137-2385-x.13).
- Jansma, P., G. Mattioli, A. Lopez, C. DeMets, T. Dixon, P. Mann, and E. Calais (2000). Neotectonics of Puerto Rico and the Virgin Islands, northeastern Caribbean, from GPS geodesy, *Tectonics* **19**, no. 6, 1021–1037.
- Kanamori, H. (1977). The energy release in great earthquakes, *J. Geophys. Res.* **82**, no. 20, 2981–2987, doi: [10.1029/JB082i020p02981](https://doi.org/10.1029/JB082i020p02981).
- Liu, C., T. Lay, Z. Wang, and X. Xiong (2020). Rupture process of the 7 January 2020, MW6.4 Puerto Rico earthquake, *Geophys. Res. Lett.* **47**, no. 12, 1–8, doi: [10.1029/2020gl087718](https://doi.org/10.1029/2020gl087718).
- López, A. M., K. S. Hughes, and E. Vanacore (2020). Puerto Rico's winter 2019–2020 seismic sequence leaves the island on edge, *Temblor*, available at <https://temblor.net/earthquake-insights/puerto-ricos-winter-2019-2020-seismic-sequence-leaves-the-island-on-edge-10321/> (last accessed August 2021).
- Manaker, D. M., E. Calais, A. M. Freed, S. T. Ali, P. Przybylski, G. Mattioli, P. Jansma, C. Prépetit, and J. B. D. Chaballier (2008). Interseismic plate coupling and strain partitioning in the Northeastern Caribbean, *Geophys. J. Int.* **174**, no. 3, 889–903, doi: [10.1111/j.1365-246x.2008.03819.x](https://doi.org/10.1111/j.1365-246x.2008.03819.x).
- Mann, P., E. Calais, J. Ruegg, C. DeMets, P. Jansma, and G. Mattioli (2002). Oblique collision in the northeastern Caribbean from GPS measurements and geological observations, *Tectonics* **21**, no. 6, 1057.
- Mann, P., F. Taylor, R. Edwards, and T. Ku (1995). Actively evolving microplate formation by oblique collision and sideways motion along strike-slip faults: An example from the northeastern Caribbean plate margin, *Tectonophysics* **246**, nos. 1/3, 1–69.
- Meade, B. J., P. M. R. DeVries, J. Faller, F. Viegas, and M. Wattenberg (2017). What is better than coulomb failure stress? A ranking of scalar static stress triggering mechanisms from Mainshock-Aftershock Pairs, *Geophys. Res. Lett.* **44**, no. 22, 11,409–11,416, doi: [10.1002/2017gl075875](https://doi.org/10.1002/2017gl075875).
- Mondziel, S., N. Grindlay, P. Mann, A. Escalona, and L. Abrams (2010). Morphology, structure, and tectonic evolution of the Mona canyon (northern Mona passage) from multibeam bathymetry, side-scan

- sonar, and seismic reflection profiles, *Tectonics* **29**, no. 2, doi: [10.1029/2008tc002441](https://doi.org/10.1029/2008tc002441).
- Nobile, A., R. Viltres, H. Vasyura-Bathke, D. Trippanera, W. Wenbin Xu, L. Passarelli, and S. Jónsson (2021). Fault parameters of the Mw 6.4 January 7, 2020, Puerto Rico earthquake estimated from teleseismic, GNSS and InSAR data, *EGU General Assembly 2021*, online, 19–30 April 2021, EGU21-11166, doi: [10.5194/egusphere-egu21-11166](https://doi.org/10.5194/egusphere-egu21-11166).
- Okada, Y. (1992). Internal deformation due to shear and tensile faults in a half-space, *Bull. Seismol. Soc. Am.* **82**, no. 2, 1018–1040.
- Pananont, P., M. W. Herman, P. Pornsopin, K. P. Furlong, S. Habangkaem, F. Waldhauser, W. Wongwai, S. Limpisawad, P. Warnitchai, S. Kosuwan, *et al.* (2017). Seismotectonics of the 2014 Chiang Rai, Thailand, earthquake sequence: 2014 Chiang Rai, Thailand, EQ Sequence, *J. Geophys. Res.* **122**, no. 8, 6367–6388, doi: [10.1002/2017JB014085](https://doi.org/10.1002/2017JB014085).
- Prentice, C. S., and P. Mann (2005). Paleoseismic study of the south Lajas fault: First documentation of an onshore Holocene fault in Puerto Rico, in *Active Tectonics of Puerto Rico, the Virgin Islands, and Offshore Areas*, P. Mann (Editor), Vol. 385, Geological Society of America, Boulder, Colorado, Special Paper, 215–222.
- Prentice, C., P. Mann, and G. Burr (2000). Prehistoric earthquakes associated with a Late Quaternary fault in the Lajas Valley, southwestern Puerto Rico, *Eos Trans. AGU* **81**, no. 48, Fall Meet. Suppl., Abstract T11B-10.
- Reasenber, P. A., and R. W. Simpson (1992). Response of regional seismicity to the static stress change produced by the Loma Prieta earthquake, *Science* **255**, no. 5052, 1687–1690, doi: [10.1126/science.255.5052.1687](https://doi.org/10.1126/science.255.5052.1687).
- Roig-Silva, C. M., E. Asencio, and J. Joyce (2013). The northwest trending north Boquerón Bay-Punta Montalva Fault Zone; A through going active fault system in southwestern Puerto Rico, *Seismol. Res. Lett.* **84**, no. 3, 538–550, doi: [10.1785/0220120115](https://doi.org/10.1785/0220120115).
- Stein, R. S., G. C. P. King, and J. Lin (1992). Change in failure stress on the southern San Andreas fault system caused by the 1992 Magnitude = 7.4 Landers earthquake, *Science* **258**, no. 5086, 1328–1332, doi: [10.1126/science.258.5086.1328](https://doi.org/10.1126/science.258.5086.1328).
- Styron, R., and M. Pagani (2020). The GEM global active faults database, *Earthq. Spectra* **36**, no. 1, 160–180, doi: [10.1177/8755293020944182](https://doi.org/10.1177/8755293020944182).
- Symithe, S., E. Calais, J. B. D. Chabaliér, R. Robertson, and M. Higgins (2015). Current block motions and strain accumulation on active faults in the Caribbean, *J. Geophys. Res.* **120**, no. 5, 3748–3774, doi: [10.1002/2014jb011779](https://doi.org/10.1002/2014jb011779).
- van Benthem, S., and R. Govers (2010). The Caribbean plate: Pulled, pushed, or dragged? *J. Geophys. Res.* **115**, no. B10, doi: [10.1029/2009jb006950](https://doi.org/10.1029/2009jb006950).
- van Gestel, J.-P., P. Mann, J. F. Dolan, and N. R. Grindlay (1998). Structure and tectonics of the upper Cenozoic Puerto Rico-Virgin Islands carbonate platform as determined from seismic reflection studies, *J. Geophys. Res.* **103**, no. B12, 30,505–30,530, doi: [10.1029/98jb02341](https://doi.org/10.1029/98jb02341).
- Wells, D. L., and K. J. Coppersmith (1994). New empirical relationships among magnitude, rupture length, rupture width, rupture area, and surface displacement, *Bull. Seismol. Soc. Am.* **84**, no. 4, 974–1002.
- Wessel, P., J. F. Luis, L. Uieda, R. Scharroo, F. Wobbe, W. H. F. Smith, and D. Tian (2019). The generic mapping tools version 6, *Geochem. Geophys. Geosys.* **20**, no. 11, 5556–5564, doi: [10.1029/2019gc008515](https://doi.org/10.1029/2019gc008515).

---

Manuscript received 18 August 2021

Published online 12 January 2022